RSC Advances

PAPER

View Article Online
View Journal | View Issue

Cite this: *RSC Adv.*, 2025, **15**, 16939

Numerical analysis of the $MASnI_3$/CZT($Se_{1-x}S_x$) interface to boost the performance *via* band offset engineering

Rasmiah S. Almufarij,[a] Muazma Jamil,[b] M. Yasir Ali,[b] M. D. Alshahrani,[c] Salhah Hamed Alrefaee,[d] Mohamed Abdelsabour Fahmy,[ef] Islam Ragab,[g] A. R. Abd-Elwahed,[h] Adnan Ali*[b] and Arslan Ashfaq *[i]

This study investigates a tin-based perovskite solar cell (PSC) incorporating an inorganic hole transport layer, examined through simulations with the SCAPS simulator. The chosen CuZnSn($Se_{1-x}S_x$) compound emerges as a promising candidate for the hole transport layer, allowing for a tunable band gap *via* adjustments to the S/(S + Se) ratio. The band gap varies from 0.95 eV for $Cu_2ZnSnSe_4$ to 1.5 eV for Cu_2ZnSnS_4, achieved through strategic valence band offset engineering at the $MAPbI_3$/CuZnSn($Se_{1-x}S_x$) interface. However, achieving an optimal Valence Band Offset (VBO) at $MASnI_3$/CuZnSn($Se_{1-x}S_x$) remains challenging yet crucial for realizing high-performance Perovskite Solar Cells. The device efficiency is systematically optimized by manipulating the S content, resulting in a noteworthy Power Conversion Efficiency of 18.29%. Furthermore, it is uncovered that a carefully selected VBO (0.22 eV) is achieved with the $CZTSe_{0.4}S_{0.6}$ hole transport layer, contributing significantly to the improved performance of the PSC. These findings underscore the importance of precise engineering in achieving optimal device properties for advanced solar energy conversion applications.

Received 31st March 2025
Accepted 13th May 2025

DOI: 10.1039/d5ra02248g

rsc.li/rsc-advances

1 Introduction

In recent years, there has been substantial progress in advancing perovskite solar cells (PSCs), a trend that began with the initial report in 2009.[1] A lot of work has gone into producing solar cells with greater efficiency, with perovskite materials emerging as one of the most promising alternatives for future developments. The power conversion efficiency (PCE) of hybrid halide perovskite has increased dramatically, from 3.8% to an astounding 25.2%, which justifies the material's increased attention on a global scale.[2,3] Metal halide perovskites, or PSCs, are represented by the formula ABX_3, where A stands for non-bonding monovalent cations, such as methylammonium $(MA)^+$, formamidinium $(FA)^+$, and cesium $(Cs)^+$; B represents octahedral divalent ions, usually Pb^{2+}; and X is a monoanionic ion, usually from the halide group (Cl^-, Br^-, I^-, or a mixture).

Compared to more known technologies such as CdTe, CIGS, and silicon solar cells, this photovoltaic (PV) breakthrough has been achieved rather quickly. Characteristics such as an appropriate band gap, high absorption coefficient, ambipolar charge-carrier transport, small exciton binding energy, long diffusion length, defects tolerance, low fabrication cost, and low effective carrier masses are responsible for PSCs success.[4,5]

Despite the remarkable accomplishments of PSCs, challenges remain for their broader adoption. Lead (Pb), a toxic element, risks human health and the natural environment.[6] Additionally, $MAPbI_3$ experiences reduced performance due to poor stability when exposed to moisture and sunlight.[7] To address these issues, various nontoxic metals such as copper, bismuth, germanium, antimony, and tin have been explored as substitutes for Pb in PSCs.[8,9] Sn has been identified as the most promising substitution for improving PSC performance.

$MASnI_3$, with its narrow band gap of 1.3 eV compared to $MAPbI_3$, exhibits a similar valency. The slight reduction in the radius of Sn^{2+} (1.35 Å) compared to Pb^{2+} (1.49 Å) allows for the replacement of Pb^{2+} with Sn^{2+} while maintaining the perovskite structure.[10] The Goldschmidt tolerance factor and octahedral

[a]*Department of Chemistry, College of Science, Princess Nourah bint Abdulrahman University, P. O. Box 84428, Riyadh 11671, Saudi Arabia*
[b]*Department of Physics, Government College University, Faisalabad, 38000, Pakistan. E-mail: adnnan_1982@yahoo.com*
[c]*Department of Physics, College of Science, University of Bisha, P. O. Box 551, Bisha 61922, Saudi Arabia*
[d]*Department of Chemistry, College of Science, Taibah University, Yanbu-30799, Madinah, Saudi Arabia*
[e]*Adham University College, Umm Al-Qura University, Adham 28653, Makkah, Saudi Arabia*
[f]*Faculty of Computers and Informatics, Suez Canal University, New Campus, 41522 Ismailia, Egypt*
[g]*Department of Chemistry, College of Science, Qassim University, 51452 Buraidah, Saudi Arabia*
[h]*Department of Physics, College of Science, Qassim University, Buraydah 51452, Saudi Arabia*
[i]*Department of Physics, Emerson University Multan, 60000, Pakistan. E-mail: arslan.ashfaq@eum.edu.pk*

factor play a critical role in assessing the structural stability and feasibility of forming perovskite phases, thereby serving as essential criteria for the rational design and selection of high-performance perovskite materials in solar cell applications.[11] Sn^{2+} substitution adheres to coordination, causes minimal lattice constant perturbation, and maintains ionic size and charge balance.[12,13] Tin-based, environmentally friendly perovskite materials hold the potential to enhance device performance and stability. However, tin-based PSCs face challenges, including sensitivity to oxygen leading to rapid oxidation of Sn^{2+} into Sn^{4+}, as well as the self-doping effect and rapid crystallization rate during solution preparation, resulting in current losses and reduced power conversion efficiency (PCE).[14,15]

Numerous techniques have emerged to enhance the performance of $MASnI_3$-based devices. For instance, adopting a n–i–p device configuration with mesoscopic TiO_2 and Spiro-OMeTAD as the hole transport material has achieved a PCE of 6.4%.[16] In 2019, $MASnI_3$ achieved a PCE of 7.19% through a normal device by employing cation exchange approaches.[17] The proper selection of electron transport materials (ETM) and hole transport materials (HTM) is crucial for improving the efficiency, reproducibility, and stability of solar cell. However, the use of organic materials such as Spiro-OMeTAD, PATT, and PEDOT:PSS poses challenges due to potential degradation and high costs, hindering the commercialization of perovskites.[18]

Inorganic copper-based HTLs, including $CuSbS_2$ and CuSCN, have been investigated for their suitable band gap and long-term stability.[19] However, the performance of devices using these materials falls short compared to their organic counterparts. To further enhance the efficiency of PSCs with in-organic HTLs, it is crucial to identify other materials with appropriate energy band positions, inherent properties, excellent chemical stability, and high conductivity.[20]

Copper-based materials possess chemical stability, high conductivity, and hole transport mobility, making them suitable candidates as HTLs in PSCs. Cu_2ZnSnS_4 is an environmentally friendly, nontoxic, and abundant material with a high absorption coefficient of 10^5 cm^{-1}, an heightened energy band gap of 1.5 eV, and excellent stability, making it viable for use in low price devices. While the maximum achieved PCE of CZTS is 9.6%, the alloying of $Cu_2ZnSn(Se_{1-x}S_x)_4$ compound has demonstrated superior performance, reaching 12.6% efficiency with a tunable band gap.[21,22] Notably, $CZTSe_{1-x}S_x$ has not only been explored as a potential light absorber in thin-film solar cells but has also shown promise as an HTL in PSCs, achieving an efficiency of 22.77%.[23] $CZTSe_{1-x}S_x$ can be synthesized using a nanoparticle ink method, eliminating the need for high-temperature sulfuration and enabling its use at lower temperatures. A study in 2016 investigated the band level alignment and valence band position influence of CZTS and CZTSe nanoparticles ink as HTL on the performance of PSCs.[24]

This manuscript introduces the novel concept of utilizing $CZTSe_{1-x}S_x$ as an HTL in $MASnI_3$ PSCs through Solar Cell Capacitance Simulator (SCAPS), marking the first time this device modeling approach has been considered. The traditional structure of PSCs is examined and discussed, focusing on the valence band offset between the perovskite light absorber and $CZTSe_{1-x}S_x$, as well as the band gap of the HTL controlled through composition engineering of the $CZTSe_{1-x}S_x$ compound. The effects of these factors on the *IV* characteristics and efficiency parameters are thoroughly investigated, leading to an optimized power conversion efficiency achieved with a specific S composition. At $CZTSe_{0.4}S_{0.6}$ composition, a notable efficiency of 17.29% is attained. Further optimization of carrier concentration, defect density, and diffusion length of tin-based

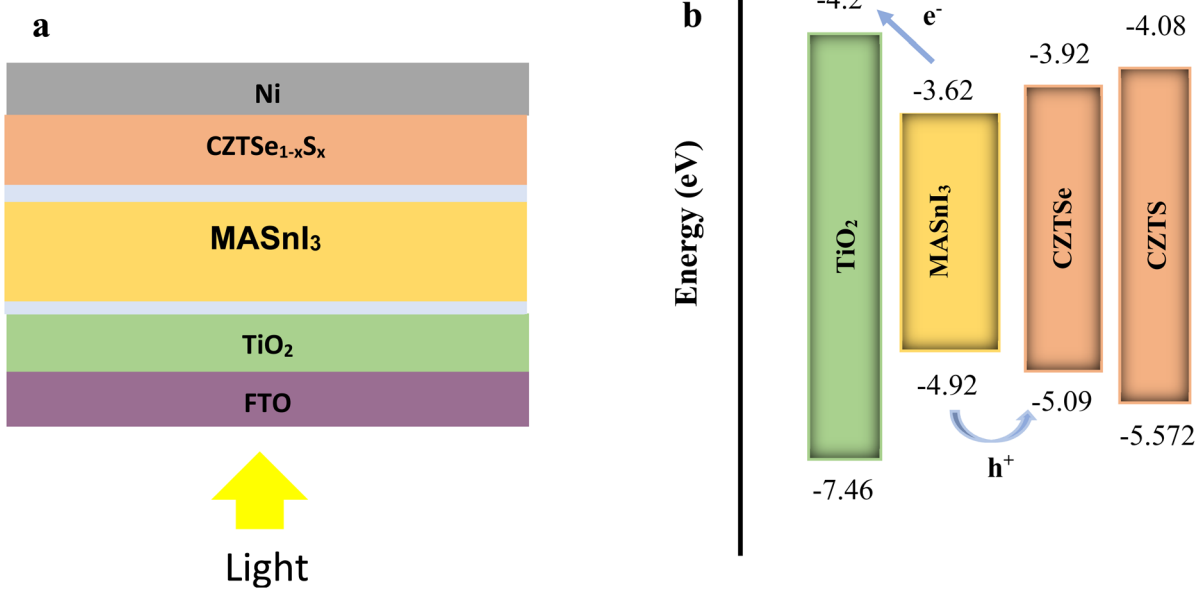

Fig. 1 (a) Architecture of modelling device (b) energy level alignment.

Table 1 The initial input parameters of the simulated device[27–29]

Parameters	FTO	TiO_2	$MASnI_3$	Spiro-OMeTAD	CZTSe	CZTS
ε_r	9	10	8.2	3.0	10	10
χ (eV)	4	4	4.17	2.45	4.35	4.5
E_g (eV)	3.5	3.2	1.3	3.0	0.95	1.5
N_c (cm^{-3})	2.2×10^{18}	2×10^{17}	1.0×10^{18}	2.2×10^{18}	2.2×10^{18}	2.2×10^{18}
N_v (cm^{-3})	1.8×10^{19}	6×10^{17}	1.0×10^{18}	1.8×10^{19}	1.8×10^{19}	1.8×10^{19}
μ_n (cm^{-2} V^{-1} s^{-1})	20	100	1.6	2×10^{-4}	60	100
μ_p (cm^{-2} V^{-1} s^{-1})	10	25	1.6	2×10^{-4}	20	25
N_a (cm^{-3})	0	0	0	2×10^{18}	5×10^{16}	5×10^{16}
N_d (cm^{-3})	2×10^{19}	2×10^{19}	2×10^{16}	10	10	10
v_e (cm s^{-1})	1×10^{7}	1×10^{7}	1×10^{7}	1×10^{7}	1×10^{7}	1×10^{7}
v_h (cm s^{-1})	1×10^{7}	1×10^{7}	1×10^{7}	1×10^{7}	1×10^{7}	1×10^{7}
d (nm)	50	50	450	200	200	200
N_t (cm^{-3})	1×10^{15}	1×10^{14}	2.5×10^{13}	1×10^{14}	1×10^{14}	1×10^{14}

Table 2 The input parameters of defect in $MASnI_3$ and interface of layers

Parameters	$MASnI_3$	TiO_2/IDL	IDL2/HTL
Defect type	Neutral	Neutral	Neutral
Capture cross section for electrons/holes (/cm^2)	2×10^{-14}	1×10^{-18}	1×10^{-18}
	2×10^{-14}	1×10^{-17}	1×10^{-19}
Energetic distribution	Gaussian	Single	Single
Energy level w.r.t E_v (above E_v, eV)	0.65	0.07	0.32
Characteristics energy/eV	0.1	—	—
Total density/cm^{-3}	Variable	1×10^{9}	1×10^{9}

perovskite in $CZTSe_{0.4}S_{0.6}$ results in an enhanced PCE of 17.34%.

2 Device configuration

The schematic representation of the simulated structure and the energy level alignment of the device structure are illustrated in Fig. 1. The cell configuration comprises a SLG substrate/FTO (used as TCO)/TiO_2 (serving as ETL)/$MASnI_3$ as the absorber/$CZTSe_{1-x}S_x$ (employed as HTL)/Ni (functioning as the back contact), as depicted in Fig. 1(a). The energy levels and electron affinities of the main layers are presented in Fig. 1(b).

The simulation of the device is conducted using SCAPS 3.310, a software developed by the Department of Electronics and Information Systems (ELIS) at the University of Gent.[25] The simulation is performed under 1 Sun illumination with an incident power density of 1 kW m^{-2} at a temperature of 300 K. SCAPS utilizes well-established equations from literature,[26] including the continuity equation, Poisson's equation, and electron/hole transport equations, to model various recombination mechanisms for solar cell simulation.

Table 1 presents fundamental parameters obtained from experimental and published data for the HTL, ETL, and FTO, as documented in sources. To represent the optical behavior of each layer accurately, the absorption coefficients for all active layers were incorporated. The absorption coefficient of $MASnI_3$ was modeled using the Tauc relation with a pre-factor $A_\alpha = 10^5$, while the absorption profiles of TiO_2 and $CZT(Se_{1-x}S_x)$ were extracted from reported experimental literature.[27,30,31] The effective density states for valence and conduction bands is established at 1.8×10^{19} and 2.2×10^{18} cm^{-3}, respectively, with the exception of the ETL.[32] The thermal velocities of holes and electrons are set at 1×10^7 cm s^{-1}. For accurate representation, $MASnI_3$ is assigned an electron carrier density of 2.0×10^{16} cm^{-3}.

To account for interface recombination, two Interface Defect Layers (IDLs) are introduced between TiO_2/perovskite and $MASnI_3$/HTL. These IDLs share identical parameters with $MASnI_3$ for consistency.

To achieve a carrier lifetime of 1 ns in the absorber layer, a defect density of 2.5×10^{13} cm^{-3} is presumed, aligning with the theoretical range of 1 ns to 4 ns. Table 2 compiles information on interface defects and absorber defects. Front optical filtration employs Transmission Solar Glass, and the back contact metal work function is set to 5.3 eV.[33]

The band gap (E_g) and electron affinity (χ) of the $CZTSe_{1-x}S_x$ HTL are adjusted according to the sulfur content (x). Previous studies indicated that the E_g values for CZTS ($x = 1$) and CZTSe ($x = 0$) were 1.5 and 0.95 eV, respectively. The determination of E_g and χ for $CZTSe_{1-x}S_x$ at various sulfur concentrations (x) is accomplished using equations from the literature.[28]

3 Results and discussion

The simulation primarily focuses on the tin-based perovskite structure with Spiro-OMeTAD as the Hole Transport Layer (HTL), aiming to compare CZTSe and CZTS, respectively. Fig. 2 illustrates the numerical simulated J–V curve of the reference

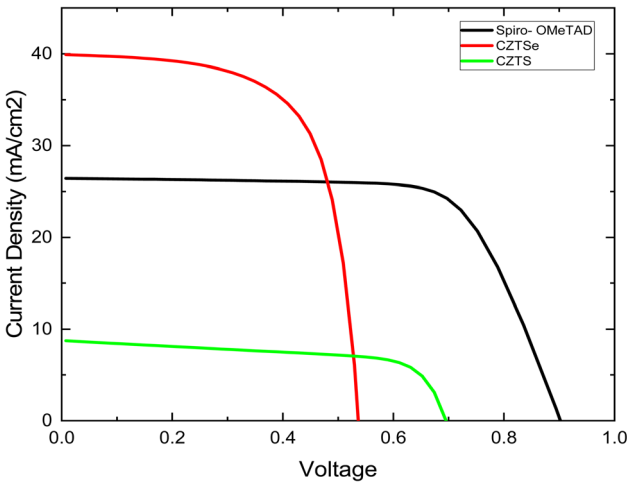

Fig. 2 The numerical simulated J–V properties of different HTL.

solar cell. The reference cell, utilizing Spiro-OMeTAD, exhibits a Power Conversion Efficiency of 23.36%, V_{oc} of 0.93 V, J_{sc} of 31.60 mA cm^{-2}, and a FF of 79.99%. These values strongly correlate with reported experimental and theoretical data for high-efficiency PSCs with performance exceeding 20%.[34,35]

In addition to the reference cell, the study explores CZTSe and CZTS as HTLs, keeping all other parameters constant except for those related to the HTL. The simulated J–V properties with CZTSe HTL show a V_{oc} of 0.52 V, J_{sc} of 39.88 mA cm^{-2}, FF of 66.28%, and an efficiency of 13.95%. Notably, all efficiency parameters in this simulation are lower than those with Spiro-OMeTAD HTL in tin-based perovskite solar cells, yet these results align with previously reported experimental outcomes. The simulations are conducted with a thickness of 200 nm and a total defect density of 5×10^{16} cm^{-3} for both CZTSe and CZTS.

Our simulation reveals that CZTSe, as an HTL, demonstrates a power conversion efficiency comparable to Spiro-OMeTAD in tin-based PSCs. This similarity is attributed to the approximately aligned band structures of $MASnI_3$/Spiro-OMeTAD and $MASnI_3$/CZTSe interfaces.

The CZTSe alloys possess the capability of a tunable energy band gap. Therefore, employing a configuration engineering method allows for the investigation of the $CZTSe_{1-x}S_x$ compound and the optimization of band alignment at interfaces, consequently influencing PCE in tin-based devices. The changes in performance of the IV parameters with different sulfur concentrations in $CZTSe_{1-x}S_x$ as the Hole Transport Layer (HTL) is depicted in Fig. 3.

Tin-based PSCs with CZTSe as the HTL exhibit relatively lower performance IV parameters. With the addition of a small fraction of S to CZTSe, J_{sc} experiences a slight decrease, followed by a more substantial decrease. As the S concentration increases up to approximately 0.6, V_{oc}, J_{sc}, and η show an increase, while FF initially decreases before starting to increase again, as shown in Fig. 3(c). Beyond $x = 0.7$, a significant decrease in all parameters is observed. Therefore, optimized performance is observed at $x = 0.6$.

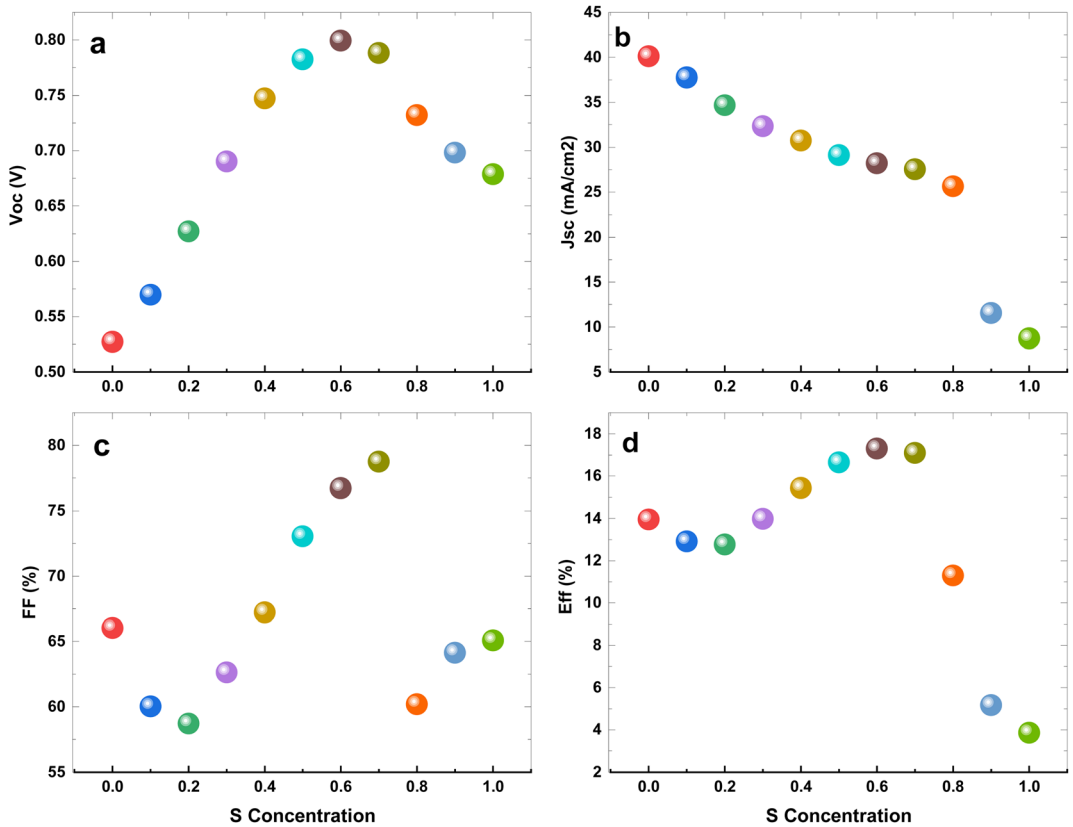

Fig. 3 The variation in the performance of the IV parameters with the different S concentration in $CZTSe_{1-x}S_x$ as HTL in structure.

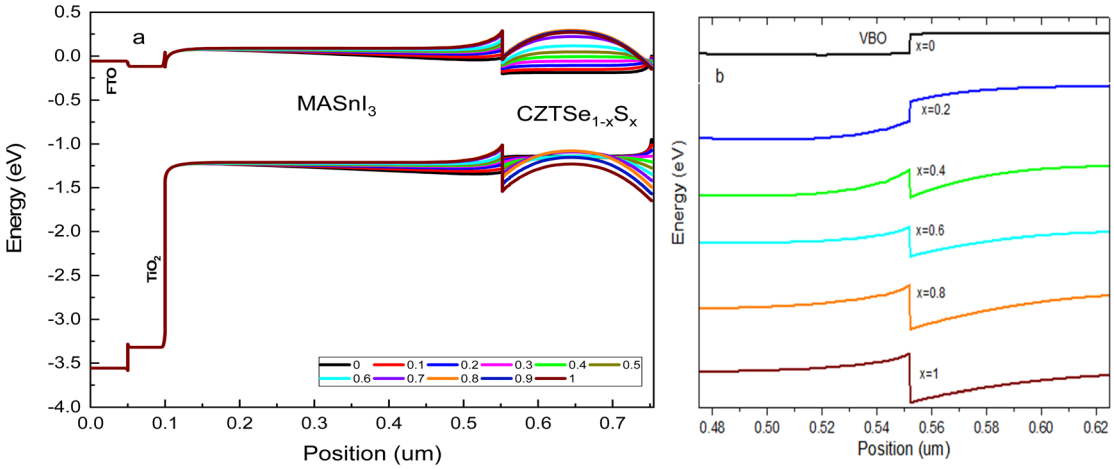

Fig. 4 (a) Energy band diagram of tin based PSCs with $CZTSe_{1-x}S_x$ HTL (b) $MASnI_3$/HTL valence band offset.

At the adjusted of the sulfur content, the tin-based PSCs demonstrate a V_{oc} of 0.79 V, J_{sc} of 28.20 mA cm^{-2}, FF of 76.71%, and PCE of 17.29%. This efficiency is in correspondence with Spiro-OMeTAD-based lead-free PSCs.

The S/(S + Se) ratio serves to control the band gap (E_g) and electron affinity (χ) of the $CZTSe_{1-x}S_x$ Hole Transport Layer (HTL). Through composition engineering, the Conduction Band Offset (CBO) and Valence Band Offset (VBO) at the interface of $MASnI_3$/$CZTSe_{1-x}S_x$ can be practically manipulated. The band diagram of $MASnI_3$ with $CZTSe_{1-x}S_x$ HTL is presented in Fig. 4(a). To facilitate the hole charge transportation from the tin-based absorber layer to the HTL, the valence energy band level of the HTL is usually slightly lower than the conduction band level of $MASnI_3$, leading to a reduction in the Built-in Potential (V_{bi}). It is related that a small negative VBO can result in a low V_{oc}. CZTSe shows a −0.17 eV VBO and the lowest V_{bi} (−0.35 V), which corresponds to the smallest V_{oc} in Fig. 3(a).

The VBO of $CZTSe_{1-x}S_x$ consistently shifts to deeper energy levels, resulting in values of VBO and V_{bi} transitioning from negative to positive with the addition of sulfur concentration in CZTSe, as indicated in Fig. 4b and 5. A positive (+ive) VBO is most favorable for reducing charge carrier recombination.[36] The complete valence energy band alignment at the $MASnI_3$/$CZTSe_{1-x}S_x$ interface is illustrated in Fig. 4(a and b) with a distinctly vertical transfer. The fluctuation in the valence energy band position of $CZTSe_{1-x}S_x$ alters the V_{bi} in the absorber layer.

The V_{bi} is defined as $V_{bi}(CZTSe_{1-x}S_x) = E_g(CZTSe_{1-x}S_x) + \Delta E_v(CZTSe_{1-x}S_x) + kT \ln\left(\frac{N_a N_d}{N_{c(CZTSe_{1-x}S_x)} N_{v(MASnI_3)}}\right)$, and the VBO $= \chi(CZTSe_{1-x}S_x) + E_g(CZTSe_{1-x}S_x) - \chi(MASnI_3) - E_g(MASnI_3)$. The values of VBO and V_{bi} are attained and depicted in Fig. 5. CZTS shows the maximum VBO (0.53 eV) and V_{bi} (0.89 V) as the VBO becomes deeper with increasing sulfur content, leading to an increase in V_{bi}. In our study, tin-based PSCs with $CZTSe_{0.6}S_{0.4}$ or $CZTSe_{0.4}S_{0.6}$ HTLs show a +ive VBO of 0.08 eV and 0.22 eV, respectively. From Fig. 5, it can be inferred that tin-based PSC with $CZTSe_{0.4}S_{0.6}$ HTL demonstrates sufficient V_{bi}, which significantly participate to the larger V_{oc} examined in Fig. 3(a).

The overall rate of generation and recombination in tin-based PSCs with $CZTSe_{1-x}S_x$ is depicted in Fig. 6. With a thickness of 450 nm for $MASnI_3$, the majority of incident light is absorbed, allowing only a small portion to be transmitted, given its large range of the absorption co-efficient (10^4–10^5 cm^{-3}). As seen in Fig. 6(a), carrier generation primarily appears in the $MASnI_3$ layer. The suitable band gap of $CZTSe_{1-x}S_x$ in the range of 0.95–1.5 eV impacts the generation rate and recombination rate of the charge carriers for the transmitted light.

When $CZTSe_{1-x}S_x$ is employed as the Hole Transport Layer (HTL), maximum charge carrier generation was examined in CZTSe. The charge carrier generation rate decreases as the sulfur content increases, attributed to the widening band gap. The interface of $MASnI_3$/$CZTSe_{1-x}S_x$, a potential barrier hinders the motion of electrons from the HTL to $MASnI_3$ due to the Conduction Band Offset (CBO). Simultaneously, the V_{bi} in the perovskite layer propels photon-generated majority charge carriers toward the $CZTSe_{1-x}S_x$, facilitating easy recombination with already available minority carriers in the $CZTSe_{1-x}S_x$.[37]

Hence, the total recombination rate in $CZTSe_{1-x}S_x$ is noted to be less than Spiro-OMeTAD. For certain concentrations, the recombination rate is particularly small due to the reduced accessibility of the recombined electrons, driven by the high sulfur concentration and an appropriate Valence Band Offset (VBO). Among the $CZTSe_{1-x}S_x$ compositions, $CZTSe_{0.4}S_{0.6}$ exhibits a slightly lower total recombination rate.

The defect density (N_t) of $MASnI_3$ is adjusted to 2.5×10^{13} cm^{-3}, aligning with the carrier diffusion length of 0.9 μm based on earlier numerical simulated investigations of prime structure. To investigate the impact of N_t further, we varied N_t from 10^{12}–10^{17} cm^{-3} and illustrated the change of I–V curves with N_t in Fig. 7. The cell demonstrates a substantial performance improvement with a decrease in N_t in tin-based perovskite, consistent with simulations of lead-based perovskite.[38] A lower N_t results in better photovoltaic performance, achieving V_{oc} of 0.80 V, J_{sc} of 29.13 mA cm^{-2}, FF of 78.31%, and PCE of 18.29%.

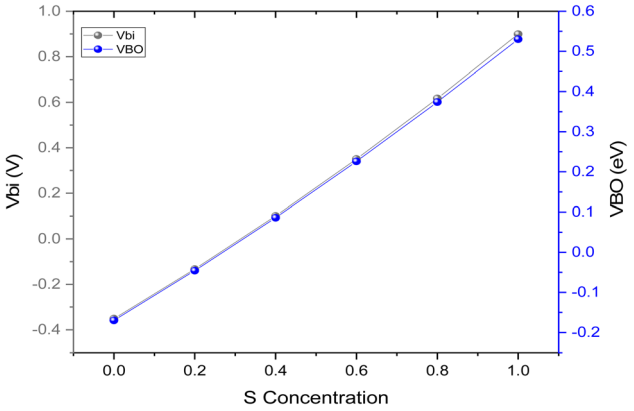

Fig. 5 The change of VBO and V_{bi} with different S content in $CZTSe_{1-x}S_x$ HTL.

Experimental literature indicates that Sn-based PSCs exhibits favorable charge-transport characteristics. To delve deeper into the effect of N_t on the device, we examine the impact of N_t on the charge carrier diffusion length (L) in Fig. 8, based on $L = \sqrt{D\tau}$ and $D = \frac{\mu kT}{q}$, where μ represents carrier mobility and is used to determine the diffusion length of carriers. Lower N_t values correspond to longer diffusion lengths (L), which contributes to the enhancement of cell performance.

Considering the influence of N_t and $l_n(l_p)$, the devices performance parameters are optimum when N_t is as low as 2.491×10^{13} cm^{-3} (resulting in a $l_n(l_p)$ of 0.9 μm), and the absorber layer thickness is 450 nm. This substantial performance improvement is attributed to the increased $l_n(l_p)$ associated with the reduction in N_t. Table 3 provides a comparative summary of $MASnI_3$-based perovskite solar cells reported in the literature along with the current simulated device. In this study, a PCE of 18.29% was achieved for the $MASnI_3/CuZnSn(Se_{1-x}S_x)$ heterostructure, demonstrating the role of optimized absorber thickness, defect passivation, and favorable band alignment through interface engineering. Notably, an experimental absorption model was employed in our simulation, resulting in

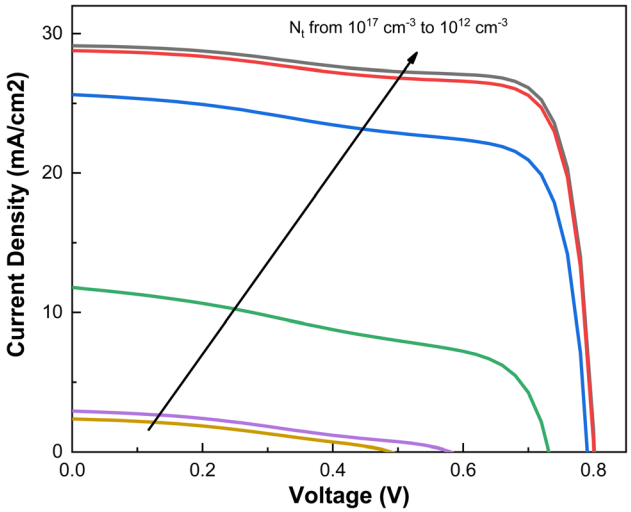

Fig. 7 Variation in I–V curves with increasing the values of N_t in $CZTSe_{0.4}S_{0.6}$.

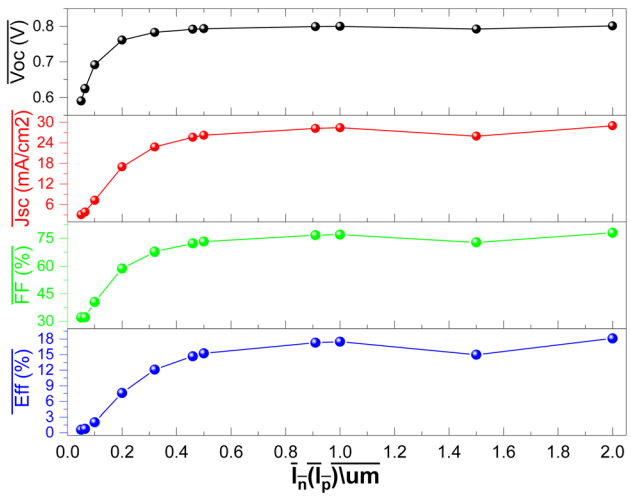

Fig. 8 Variation in device efficiency, with rising diffusion length in $MASnI_3/CZTSe_{0.4}S_{0.6}$.

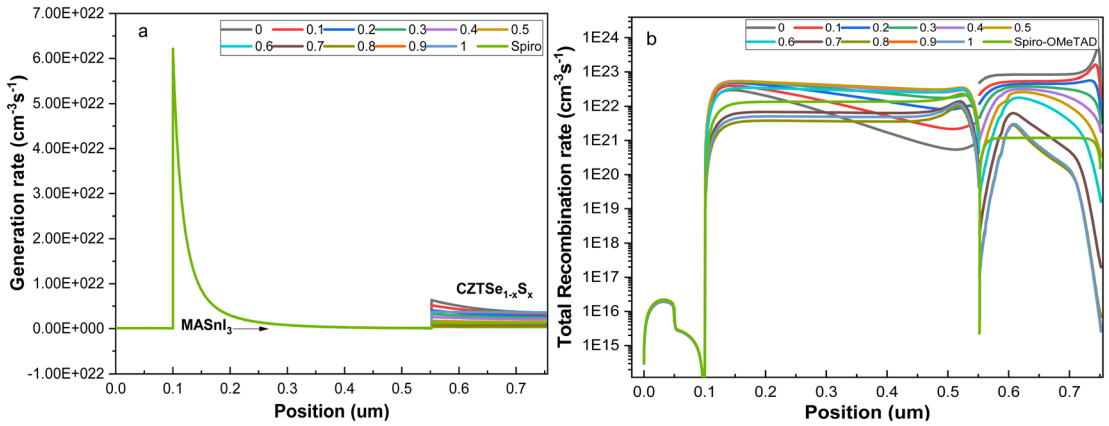

Fig. 6 The recombination rate and charge carrier generation of the PSCs with $CZTSe_{1-x}S_x$ HTL.

Table 3 Comparative performance of $MASnI_3$-based perovskite solar cells reported in the literature and the material and interface engineering

Absorber material	Device structure	PCE (%)	References
$MASnI_3$	$MASnI_3/CuZnSn(Se_{1-x}S_x)$	18.29	This work
$MASnI_3$	$PCBM/MASnI_3/CuI$	25.05	39
$MASnI_3$	$MASnI_3/CuSCN$	20.17	40
$MASnI_3$	$p\text{-}P3HT/p\text{-}MASnI_3$	22.46	41
$MASnI_3$	$BaTiO_3/MASnI_3/CuO$	24.28	42
$MASnI_3$	$BaTiO_3/MASnI_3/MASnBr_3$	24.09	42

more realistic and experimentally relevant efficiency values. In contrast, many reported studies rely on idealized absorption assumptions, often overestimating performance. Although some literature devices show higher PCEs (*e.g.*, 25.05% with CuI HTL, 24.28% using $BaTiO_3$/CuO interfaces), they typically incorporate more complex or less stable components. Our proposed structure offers a cost-effective, stable, and environmentally friendly architecture, providing a promising foundation for experimental fabrication and further optimization of high-efficiency, lead-free perovskite solar cells.

4 Conclusion

This study explores a Sn-based PSCs with an inorganic HTL, utilizing the SCAPS simulator. The compound $Cu_2ZnSn(Se_{1-x}S_x)_4$ emerges as a promising candidate for the HTL in tin-based PSCs, offering a tunable band gap through changing the S/(S + Se) ratio. This range spans from 0.95 eV for $Cu_2ZnSnSe_4$ to 1.5 eV for Cu_2ZnSnS_4, achieved through appropriate VBO engineering at the $MAPbI_3/CuZnSn(Se_{1-x}S_x)$ interface. Achieving a proper VBO at $MASnI_3/CuZnSn(Se_{1-x}S_x)$ is challenging but crucial for obtaining high-performance PSCs. Optimization of solar cell performance is carried out by adjusting the S concentration, resulting in PCE of 18.29%. Additionally, it is revealed that an appropriate VBO (0.22 eV) is achieved with the $CZTSe_{0.4}S_{0.6}$ hole transport layer, contributing to enhanced PSC performance.

Data availability

Data available on suitable request.

Conflicts of interest

There are no conflicts to declare.

Acknowledgements

The authors would like to thank Princess Nourah bint Abdulrahman University Researchers Supporting Project number (PNURSP2025R316), Princess Nourah bint Abdulrahman University, Riyadh, Saudi Arabia for funding this research article.

References

1 A. Kojima, K. Teshima, Y. Shirai and T. Miyasaka, Organometal halide perovskites as visible-light sensitizers for photovoltaic cells, *J. Am. Chem. Soc.*, 2009, **131**, 6050–6051.
2 D. Yang, R. Yang, K. Wang, C. Wu, X. Zhu, J. Feng, X. Ren, G. Fang, S. Priya and S. Liu, High efficiency planar-type perovskite solar cells with negligible hysteresis using EDTA-complexed SnO2, *Nat. Commun.*, 2018, **9**, 3239.
3 Q. Jiang, L. Zhang, H. Wang, X. Yang, J. Meng, H. Liu, Z. Yin, J. Wu, X. Zhang and J. You, Enhanced electron extraction using SnO2 for high-efficiency planar-structure HC (NH2) 2PbI3-based perovskite solar cells, *Nat. Energy*, 2016, **2**, 1–7.
4 S. Sun, T. Salim, N. Mathews, M. Duchamp, C. Boothroyd, G. Xing, T. C. Sum and Y. M. Lam, The origin of high efficiency in low-temperature solution-processable bilayer organometal halide hybrid solar cells, *Energy Environ. Sci.*, 2014, **7**, 399–407.
5 C. Wehrenfennig, G. E. Eperon, M. B. Johnston, H. J. Snaith and L. M. Herz, High charge carrier mobilities and lifetimes in organolead trihalide perovskites, *Adv. Mater.*, 2013, **26**, 1584.
6 A. Babayigit, A. Ethirajan, M. Muller and B. Conings, Toxicity of organometal halide perovskite solar cells, *Nat. Mater.*, 2016, **15**, 247–251.
7 G. Nagabhushana, R. Shivaramaiah and A. Navrotsky, Direct calorimetric verification of thermodynamic instability of lead halide hybrid perovskites, *Proc. Natl. Acad. Sci. U. S. A.*, 2016, **113**, 7717–7721.
8 M. Jahandar, J. H. Heo, C. E. Song, K.-J. Kong, W. S. Shin, J.-C. Lee, S. H. Im and S.-J. Moon, Highly efficient metal halide substituted CH3NH3I (PbI2) 1− X (CuBr2) X planar perovskite solar cells, *Nano Energy*, 2016, **27**, 330–339.
9 F. Li, Y. Wang, K. Xia, R. L. Hoye and V. Pecunia, Microstructural and photoconversion efficiency enhancement of compact films of lead-free perovskite derivative Rb 3 Sb 2 I 9, *J. Mater. Chem. A*, 2020, **8**, 4396–4406.
10 F. Hao, C. C. Stoumpos, D. H. Cao, R. P. Chang and M. G. Kanatzidis, Lead-free solid-state organic–inorganic halide perovskite solar cells, *Nat. Photonics*, 2014, **8**, 489–494.
11 K. Sekar, R. Manisekaran, O. M. Nwakanma and M. Babudurai, Significance of Formamidinium Incorporation in Perovskite Composition and Its Impact on Solar Cell Efficiency: A Mini-Review, *Adv. Energy Sustainability Res.*, 2024, **5**, 2400003.
12 B. Saparov, J.-P. Sun, W. Meng, Z. Xiao, H.-S. Duan, O. Gunawan, D. Shin, I. G. Hill, Y. Yan and D. B. Mitzi, Thin-film deposition and characterization of a Sn-deficient perovskite derivative Cs2SnI6, *Chem. Mater.*, 2016, **28**, 2315–2322.
13 W. Li, Z. Wang, F. Deschler, S. Gao, R. H. Friend and A. K. Cheetham, Chemically diverse and multifunctional hybrid organic–inorganic perovskites, *Nat. Rev. Mater.*, 2017, **2**, 1–18.
14 T. Yokoyama, D. H. Cao, C. C. Stoumpos, T.-B. Song, Y. Sato, S. Aramaki and M. G. Kanatzidis, Overcoming short-circuit in lead-free CH3NH3SnI3 perovskite solar cells via

kinetically controlled gas–solid reaction film fabrication process, *J. Phys. Chem. Lett.*, 2016, **7**, 776–782.

15 K. Chen, P. Wu, W. Yang, R. Su, D. Luo, X. Yang, Y. Tu, R. Zhu and Q. Gong, Low-dimensional perovskite interlayer for highly efficient lead-free formamidinium tin iodide perovskite solar cells, *Nano Energy*, 2018, **49**, 411–418.

16 N. K. Noel, S. D. Stranks, A. Abate, C. Wehrenfennig, S. Guarnera, A.-A. Haghighirad, A. Sadhanala, G. E. Eperon, S. K. Pathak and M. B. Johnston, Lead-free organic–inorganic tin halide perovskites for photovoltaic applications, *Energy Environ. Sci.*, 2014, **7**, 3061–3068.

17 F. Li, C. Zhang, J. H. Huang, H. Fan, H. Wang, P. Wang, C. Zhan, C. M. Liu, X. Li and L. M. Yang, A cation-exchange approach for the fabrication of efficient methylammonium tin iodide perovskite solar cells, *Angew. Chem., Int. Ed.*, 2019, **58**, 6688–6692.

18 R. S. Sanchez and E. Mas-Marza, Light-induced effects on Spiro-OMeTAD films and hybrid lead halide perovskite solar cells, *Sol. Energy Mater. Sol. Cells*, 2016, **158**, 189–194.

19 C. Devi and R. Mehra, Device simulation of lead-free MASnI 3 solar cell with CuSbS 2 (copper antimony sulfide), *J. Mater. Sci.*, 2019, **54**, 5615–5624.

20 J. Liang, J. Liu and Z. Jin, All-inorganic halide perovskites for optoelectronics: progress and prospects, *Sol. RRL*, 2017, **1**, 1700086.

21 Y. Zhang, Z. Zhang, Y. Liu, Y. Liu, H. Gao and Y. Mao, An inorganic hole-transport material of CuInSe2 for stable and efficient perovskite solar cells, *Org. Electron.*, 2019, **67**, 168–174.

22 W. Wang, M. T. Winkler, O. Gunawan, T. Gokmen, T. K. Todorov, Y. Zhu and D. B. Mitzi, Device characteristics of CZTSSe thin-film solar cells with 12.6% efficiency, *Adv. Energy Mater.*, 2014, **4**, 7.

23 N. Cheng, W. Li, S. Sun, Z. Zhao, Z. Xiao, Z. Sun, W. Zi and L. Fang, A simulation study of valence band offset engineering at the perovskite/Cu2ZnSn (Se1-xSx) 4 interface for enhanced performance, *Mater. Sci. Semicond. Process.*, 2019, **90**, 59–64.

24 M. Yuan, X. Zhang, J. Kong, W. Zhou, Z. Zhou, Q. Tian, Y. Meng, S. Wu and D. Kou, Controlling the band gap to improve open-circuit voltage in metal chalcogenide based perovskite solar cells, *Electrochim. Acta*, 2016, **215**, 374–379.

25 M. Burgelman, P. Nollet and S. Degrave, Modelling polycrystalline semiconductor solar cells, *Thin Solid Films*, 2000, **361**, 527–532.

26 A. B. Coulibaly, S. O. Oyedele and B. Aka, Comparative study of lead-free perovskite solar cells using different hole transporter materials, *Model. Numer. Simul. Mater. Sci.*, 2019, **9**, 97–107.

27 A. Mebadi, M. Houshmand, M. H. Zandi and N. E. Gorji, Numerical analysis of TiO2/Cu2ZnSnS4 nanostructured PV using SCAPS-1D, *Nano Hybrids*, 2014, **8**, 27–38.

28 M. Jamil, A. Ali, K. Mahmood, M. I. Arshad, S. Tahir, M. A. un Nabi, S. Ikram, N. Amin and S. Hussain, Numerical simulation of perovskite/Cu2Zn (Sn1-x Gex) S4 interface to enhance the efficiency by valence band offset engineering, *J. Alloys Compd.*, 2020, **821**, 153221.

29 Q.-Y. Chen, Y. Huang, P.-R. Huang, T. Ma, C. Cao and Y. He, Electronegativity explanation on the efficiency-enhancing mechanism of the hybrid inorganic–organic perovskite ABX3 from first-principles study, *Chin. Phys. B*, 2015, **25**, 027104.

30 S. Mohammadnejad and A. Baghban Parashkouh, CZTSSe solar cell efficiency improvement using a new band-gap grading model in absorber layer, *Appl. Phys. A*, 2017, **123**, 758.

31 O. Simya, A. Mahaboobbatcha and K. Balachander, Compositional grading of CZTSSe alloy using exponential and uniform grading laws in SCAPS-ID simulation, *Superlattices Microstruct.*, 2016, **92**, 285–293.

32 T. Minemoto and M. Murata, Impact of work function of back contact of perovskite solar cells without hole transport material analyzed by device simulation, *Curr. Appl Phys.*, 2014, **14**, 1428–1433.

33 J. Hölzl and F. K. Schulte, Work function of metals, *Solid Surface Physics*, 2006, 1–150.

34 H.-J. Du, W.-C. Wang and J.-Z. Zhu, Device simulation of lead-free CH3NH3SnI3 perovskite solar cells with high efficiency, *Chin. Phys. B*, 2016, **25**, 108802.

35 W. S. Yang, B.-W. Park, E. H. Jung, N. J. Jeon, Y. C. Kim, D. U. Lee, S. S. Shin, J. Seo, E. K. Kim and J. H. Noh, Iodide management in formamidinium-lead-halide–based perovskite layers for efficient solar cells, *Science*, 2017, **356**, 1376–1379.

36 T. Minemoto and M. Murata, Theoretical analysis on effect of band offsets in perovskite solar cells, *Sol. Energy Mater. Sol. Cells*, 2015, **133**, 8–14.

37 K. Sekar, L. Marasamy, S. Mayarambakam, H. Hawashin, M. Nour and J. Bouclé, Lead-free, formamidinium germanium-antimony halide (FA 4 GeSbCl 12) double perovskite solar cells: the effects of band offsets, *RSC Adv.*, 2023, **13**, 25483–25496.

38 F. Hao, C. C. Stoumpos, R. P. Chang and M. G. Kanatzidis, Anomalous band gap behavior in mixed Sn and Pb perovskites enables broadening of absorption spectrum in solar cells, *J. Am. Chem. Soc.*, 2014, **136**, 8094–8099.

39 K. D. Jayan and V. Sebastian, Comprehensive device modelling and performance analysis of MASnI3 based perovskite solar cells with diverse ETM, HTM and back metal contacts, *Sol. Energy*, 2021, **217**, 40–48.

40 S. M. Hasnain, A. Iqbal, I. Qasim, K. Irshad, M. A. Mir, M. I. Malik and L. S. Sundar, Performance evaluation of organometal halide MASnI3 and inorganic BaZrS3 hybrids in perovskites solar cells: Theoretical approach, *Hybrid Adv.*, 2025, **9**, 100408.

41 A. Najim, L. Moulaoui, A. Laassouli, O. Bajjou and K. Rahmani, Design and simulation of an organic–inorganic GO/P3HT/MASnI3 solar cell using the SCAPS-1D program, *Electr. Eng.*, 2025, 1–15.

42 S. Vaishnavi and G. Seetharaman, Computational modelling and photovoltaic performance evaluation of various ETL/HTL engineered MASnI3 planar perovskite solar cell architectures using SCAPS-1D, *Energy Convers. Manage.*, 2025, **332**, 119747.